nature portfolio

https://doi.org/10.1038/s41586-023-06652-x

Supplementary information

Dynamic diagnosis of metamaterials through laser-induced vibrational signatures

In the format provided by the authors and unedited

Supplementary Information

Dynamic Diagnosis of Metamaterials via Laser-Induced Vibrational Signatures

Yun Kai, Somayajulu Dhulipala, Rachel Sun, Jet Lem, Washington DeLima, Thomas Pezeril & Carlos M. Portela

---

CONTENTS

I. Calibration of the Interferometer

The phase mask interferometer [1] is a common-path interferometer, different than the conventional Michelson interferometer, but with analogous physical principles to translate the observable photovoltage to a displacement value. The laser intensity on the detection plane is determined as

$$I = I_1 + I_2 + 2\sqrt{I_1 I_2}\cos(\Delta\theta), \tag{1}$$

with I_1 and I_2 denoting the intensity of the two interferometric arms, respectively, and $\Delta\theta$ corresponding to their phase difference. These intensities correspond to the first-order diffraction of the phase mask, which results in equal intensity $I_1 = I_2$, defined as I_0 for simplicity, resulting in intensity expression

$$I = 2I_0 + 2I_0\cos(\Delta\theta) = 2I_0(1 + \cos(\Delta\theta)) = 4I_0\cos^2(\frac{\theta}{2}). \tag{2}$$

Translating this expression to the photodiode's laser intensity observable, i.e, photovoltage U (varying linearly with intensity), Eq. 2 can be expressed as

$$U = U_0 \cos^2(\frac{\theta}{2}) = \frac{U_0}{2} + \frac{U_0}{2}\cos(\Delta\theta). \tag{3}$$

We define U_0 as the photovoltage range, corresponding to the intensity range $4I_0$. This photovoltage range is determined by applying an electro-optics to swiftly modulate the continuous-wave (CW) probe laser intensity as a sinusoidal function so that the difference between the maximum and minimum photovoltage (thus U_0) can be determined. The modulation frequency must be higher than the AC-coupled photodetector, which is 50 kHz in our case. If the reader uses another photodetector, one must modulate the probe laser with a frequency higher than the low-frequency cut-off of that specific photodetector. Ideally, laser modulations should be done in the actual frequency range of the relevant experiments.

In practice, we manually introduce a phase difference of $\pi/2$ between the two arms by moving the phase mask up or down relative to the laser. In this scenario, Eq. 3 becomes

$$U = \frac{U_0}{2} + \frac{U_0}{2}\cos(\Delta\theta - \frac{\pi}{2}) = \frac{U_0}{2} + \frac{U_0}{2}\sin(\Delta\theta). \tag{4}$$

Furthermore, in an oscilloscope, we give the signal a voltage offset, so that when $\Delta\theta = 0$, $U = 0$, allowing Eq. 4 to be expressed as

$$U = \frac{U_0}{2}\sin(\Delta\theta), \tag{5}$$

allowing the phase difference between two interferometric arms to be derived from the experimentally measured photovoltage U as

$$\Delta\theta = \sin^{-1}\left(\frac{2U}{U_0}\right). \tag{6}$$

The phase difference is related to optical path difference γ through $\Delta\theta = 2\pi\gamma/\lambda$, where λ is the laser wavelength. Due to reflection detection, γ is twice the sample-surface displacement u. Therefore, the final expression to translate photovoltage to displacement is provided as

$$u = \frac{\lambda}{4\pi}\sin^{-1}\left(\frac{2U}{U_0}\right). \tag{7}$$

II. LIRAS High-Throughput Characterization

To further describe the LIRAS-measurements time estimates from the main text, and validate the

method's categorization as high-throughput, here we present additional details of the LIRAS measurement procedure. As mentioned int he text, the reported time needed to measure one metamaterial sample is typically between 1 to 5 minutes, which is a conservative *upper bound* for two reasons: (i) the measurement time is dictated by our choice to collect 10^4 measurements per sample, which get averaged into the final signal; and (ii) the averaging rate is determined by our specific oscilloscope speed, which inevitably averages signals slower than the 1 kHz rate at which we excite the samples. Thus, LIRAS measurements can indeed be performed in less than 1 minute if fewer measurements per sample are taken (a minor compromise in signal-to-noise ratio), and a higher-end oscilloscope is used. To provide a better sense of how time is spent in the time range we report, we timed ourselves performing experiments and produced Supplementary Fig. 1. In addition, we present a comparison between taking 1 to 512 repeated measurements on a given sample, showing that primary information such as the eigenfrequency is still determined with as little as a single measurement. As shown in Supplementary Fig. 2 below, a large majority of the analysis in this work could have been done with mere 10^1 or 10^2 measurements, but we opted for 10^4 due to its benefits in reducing experimental uncertainty.

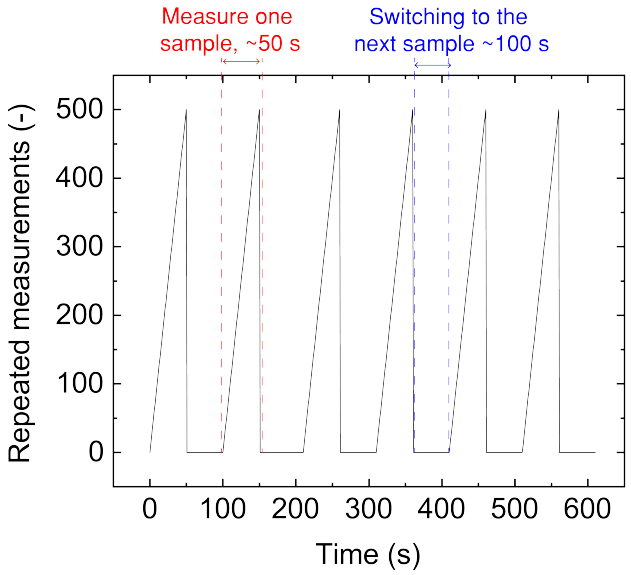

Supplementary Figure 1 | Time stamp of LIRAS experiments. Measurement-time and idle-time (switching from a measured sample to the next) are specified, demonstrating the throughput of the LIRAS method. This measurement is conducted on a pump laser with a 10 Hz repetition rate (instead of 1 kHz as in the main text) for demonstration purposes, where the read-out speed of a low-cost oscilloscope can keep up with the repetition rate of the laser.

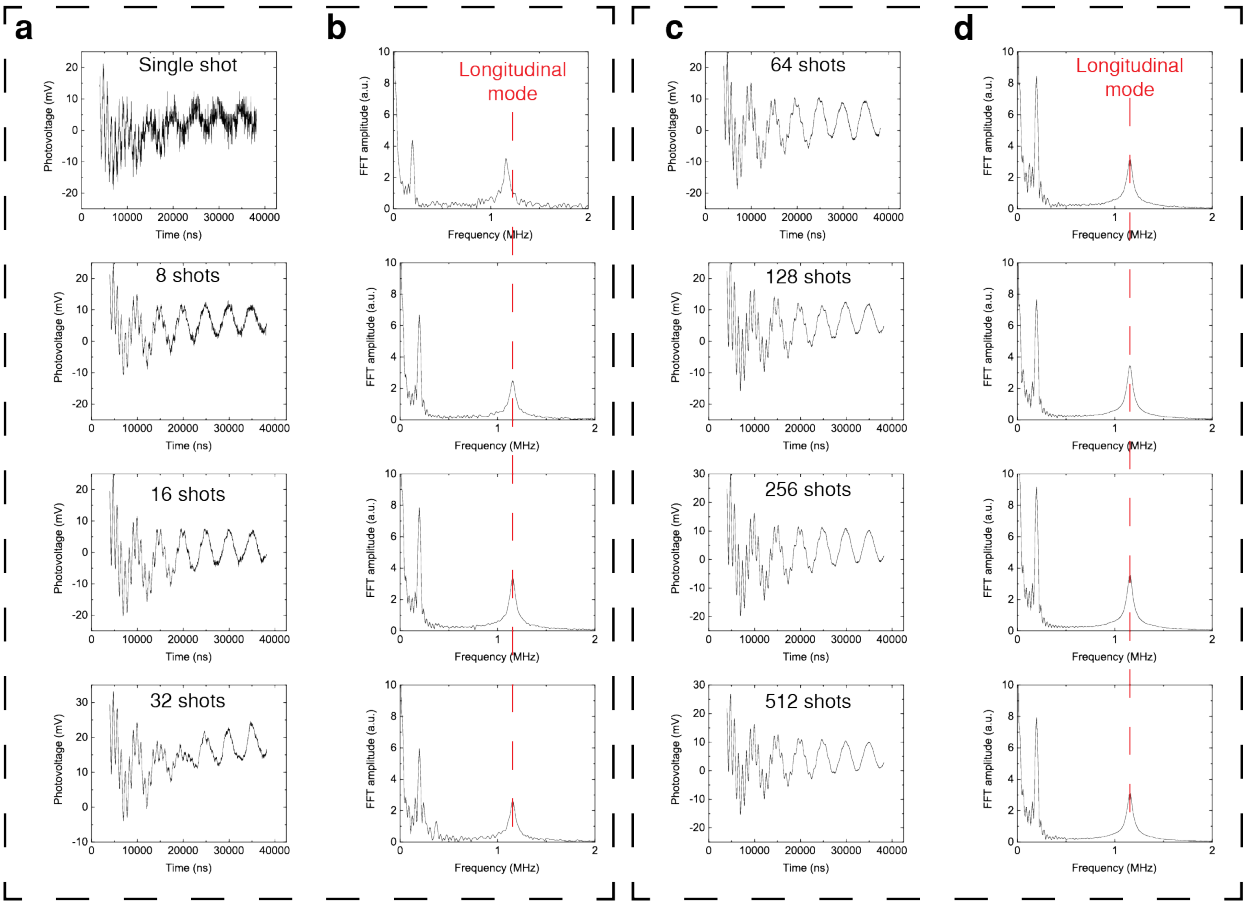

Supplementary Figure 2 | Comparison between different amounts of repeated measurements. a, Waveforms and **b**, corresponding acoustic spectra of measurements with 1 (single) to 32 shots. **c**, Waveforms and **d**, corresponding acoustic spectra of measurements with 64 to 512 shots. We employ the term "shots" to indicate the number of discrete pump laser pulses employed to obtain a given averaged waveform. Above 16 shots, no shifts in the spectral line of the longitudinal mode are detected, although the waveforms and spectra have improved signal-to-noise ratio with increasing amounts of repeated measurements.

III. Fundamental-Mode Strain and Strain-Rate Analysis and Approximations

To place the dynamic mechanical properties measured by LIRAS in a deformation and rate-of-deformation regime, we sought to determine the level of strain and strain rate induced by photoacoustic excitation. Measurement of the displacement amplitude at the top of the samples thus enabled relating the vibrational frequency with a deformation and its rate.

The displacement of any particle in our rod-geometry sample in space and time is given by

$$u(x,t) = \Gamma(t)\Phi(x), \tag{8}$$

with $\Gamma(t)$ denoting the time-varying amplitude and its decay, and $\Phi(x)$ corresponding to the spatial variation in displacement corresponding to a resonant mode. For the fundamental longitudi-

nal mode with the boundary conditions pertinent to LIRAS experiments, i.e., for a cantilevered bar with the quarter-wavelength eigenmode follows the form $\Phi(x) = \sin\left(\frac{\pi}{2}\frac{x}{H}\right)$, with H being the height of a sample. Since the fundamental longitudinal mode is identified to be the primary response in the center-pump scheme experiments—where we aim to extract information on strain and its rate—restricting this analysis to this mode is an appropriate approximation. The temporal component of $u(x,t)$ is thus the classical solution for a damped harmonic oscillator, namely $\Gamma(t) = Ae^{-\beta t}\cos(2\pi f t - \delta)$.

Following this exact solution, the effective strain within a sample is

$$\varepsilon(x,t) = u' = \frac{du(x,t)}{dx} = \Gamma(t)\Phi'(x), \tag{9}$$

where ($'$) denotes a spatial derivative, while the strain rate follows as

$$\dot{\varepsilon}(x,t) = \frac{d}{dt}\left(\frac{du(x,t)}{dx}\right) = \dot{\Gamma}(t)\Phi'(x), \tag{10}$$

with ($\dot{}$) denoting a time derivative.

To simplify our analysis of these experiments, we approximate the displacement within a sample to linearly vary from its maximum amplitude at the free end to zero at the substrate as shown as a dotted red line in Supplementary Fig. 3c, enabling computation of strain as $\varepsilon(t) \approx \frac{u(H,t)}{H}$. Thus, this approximation enables estimation of an effective strain within the sample that is within the maximum and minimum bounds of the exact solution, simplifying the analysis by removing the spatial dependence for a measure of strain. We note that while the exact solution will indeed vary in space and time, we deem this to be a reasonable approximation for the purposes of placing our LIRAS experiments in an effective strain rate regime. As discussed in Supplementary Information Section IV, computation of the time-varying effective strain rate in LIRAS experiments can thus be approximated as $\dot{\varepsilon}(t) \approx \frac{d}{dt}\left(\frac{u(H,t)}{H}\right)$.

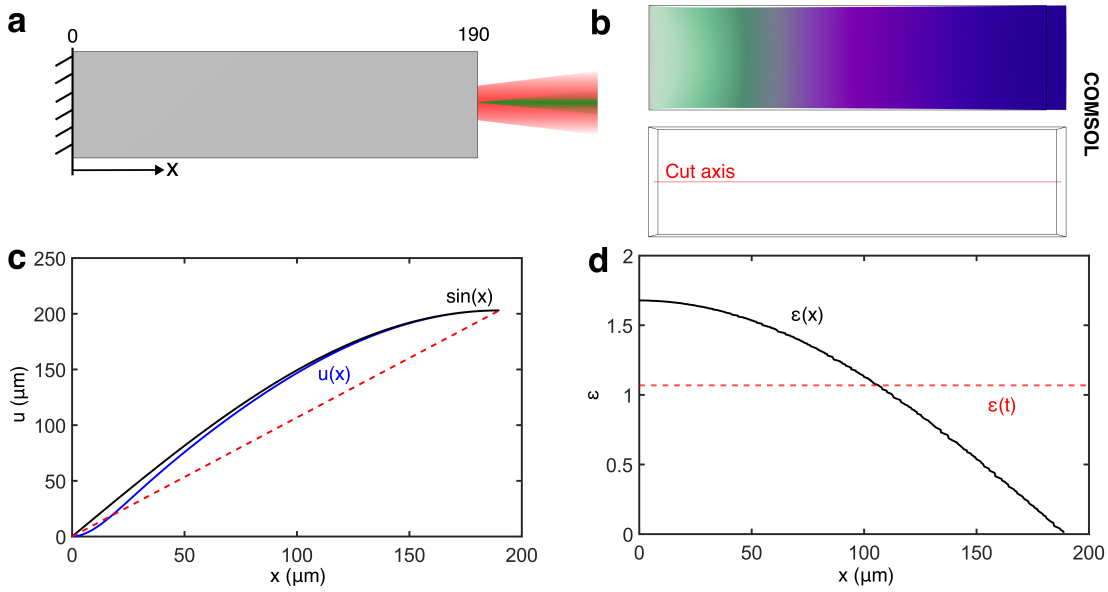

Supplementary Figure 3 | Fundamental-mode strain approximation. **a**, Rod geometry and boundary conditions. **b**, COMSOL simulation result of longitudinal mode at 2.82 MHz and cut axis across at which results are extracted. **c**, Simulation displacement $u(x)$ versus x-coordinate and its sine wave and linear (dashed red line) approximations. **d**, Exact spatial strain $\varepsilon(x)$ and time-dependent constant-strain approximation $\varepsilon(t)$ as functions of x-coordinate.

IV. Effective Strain Rate Calculation

Here, we define the effective strain rate as the RMS strain rate obtained from the strain rate-time plot. The strain rate-time data is obtained by taking a time-derivative of the time-displacement plot as shown in Extended Data Fig. 3 and dividing it by the height of the structure. The RMS strain rate between the start of the waveform T_0 and the end T_∞ is defined as

$$\dot{\varepsilon}_{RMS} = \sqrt{\frac{1}{T_\infty - T_0}\int_{T_0}^{T_\infty} \dot{\varepsilon}^2 dt}. \tag{11}$$

To compute the higher and lower limits of the effective strain rate for a given sample, we calculated the RMS strain rate from the first wavelength of the waveform (high) and the RMS strain rate for the last wavelength that is above the noise floor (low). The expressions for these high and low strain rates are

$$\dot{\varepsilon}_{h,RMS} = \sqrt{\frac{1}{T_\lambda - T_0}\int_{T_0}^{T_\lambda} \dot{\varepsilon}^2 dt}, \tag{12}$$

and

$$\dot{\varepsilon}_{l,RMS} = \sqrt{\frac{1}{T_\infty - T_{\infty-\lambda}}\int_{T_{\infty-\lambda}}^{T_\infty} \dot{\varepsilon}^2 dt}, \tag{13}$$

respectively, where T_λ denotes the time at the end of the first cycle and $T_{\infty-\lambda}$ is the time one cycle away from the end of the waveform. Finally, to obtain the characteristic strain rate for each lattice structure we average the calculated RMS quantities over the tallest 5 samples, which pertain to the long-wavelength limit.

It must be noted that the effective strain rate calculated in this section attempts to establish a *approximate* correlation between the effective stiffness obtained through LIRAS and that obtained from conventional contact-based methods. In these contact-based methods, the *constant* strain rate can be adjusted by altering the velocity of the indenter tip, allowing for a definition of strain rate as the indenter-tip velocity (ideally constant) divided by the sample height. However, such tunability in constant strain rates is not feasible in LIRAS experiments (based on principles of free-vibration with damping), but rather is determined by the samples' eigenfrequencies and indirectly by the pump laser power/vibration amplitude. The shaded range of LIRAS strain rates in Fig. 3b indicates the frequencies achievable in the samples used in the present study (based on their length scale and geometric properties). As explained in this section and Extended Data Fig. 7, a given metamaterial sample experiences a range of strain rates due to the sinusoidal displacement pattern and the ensuing attenuation. Therefore, the definition of an RMS strain rate is an attempt to place our LIRAS experiments within a context of classical characterization techniques—while keeping into consideration that a range of strain rates are actually at play.

As shown in Fig. 3b, we demonstrated that all LIRAS properties fall within less than 10% of the properties measured via constant-strain-rate contact methods, but we note that the excitation is markedly different. We have replicated Fig. 3b from the main text as Supplementary Fig. 4 in this section, including a modification that corresponds to 95% confidence intervals for the uniaxial compression fits across all samples. This figure demonstrates that by considering both the variance in effective strain rate across a single LIRAS experiment and the statistical significance of the contact-based fits, there exists a correspondence between all the data gathered from LIRAS and the data acquired from high-strain-rate uniaxial compression experiments. While the octet-metamaterial LIRAS measurements fall within a lower part of the confidence intervals (in comparison to the monolithic and tetrakaidecahedron metamaterials), these data points are statistically in agreement with the uniaxial experiments (again, despite the difference in strain rates between experiments which could lead to slightly different properties). Specifically, the LIRAS result range for the octet metamaterials is within ~8% of the uniaxial fit centerline, which is still a remarkable agreement despite the differences.

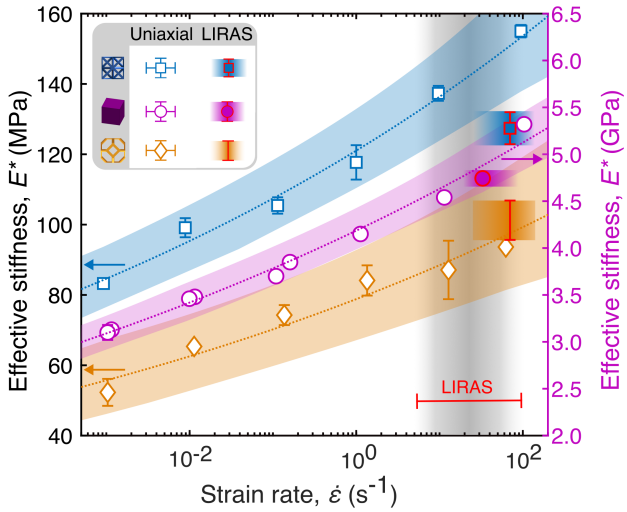

Supplementary Figure 4 | Comparison of LIRAS variable-strain-rate response to uniaxial constant-strain-rate response. Reproduction of Fig. 3b from the main text with 95% confidence intervals for the uniaxial compression fit (shaded region), denoting LIRAS experiments overlapping with confidence intervals.

V. Damped Harmonic Oscillator Analysis

Following the classical theory for harmonic motion[2], we approximate the samples in this study to behave as a single-degree-of-freedom damped harmonic oscillator, particularly in the case of longitudinal fundamental-mode vibration. As a model system, we select the Kelvin-Voigt model, consisting of a viscous dashpot and an elastic spring connected in parallel. To determine the free-vibration equation of motion of a point in this system, we represent our samples via the model depicted in Supplementary Fig. 5.

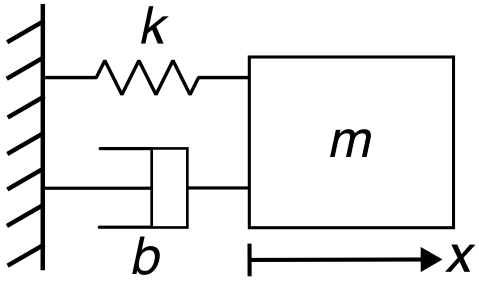

Supplementary Figure 5 | Single degree-of-freedom damped harmonic oscillator.

Establishing the equilibrium of such a system yields the equation of motion

$$m\ddot{x} = -kx - b\dot{x}, \tag{14}$$

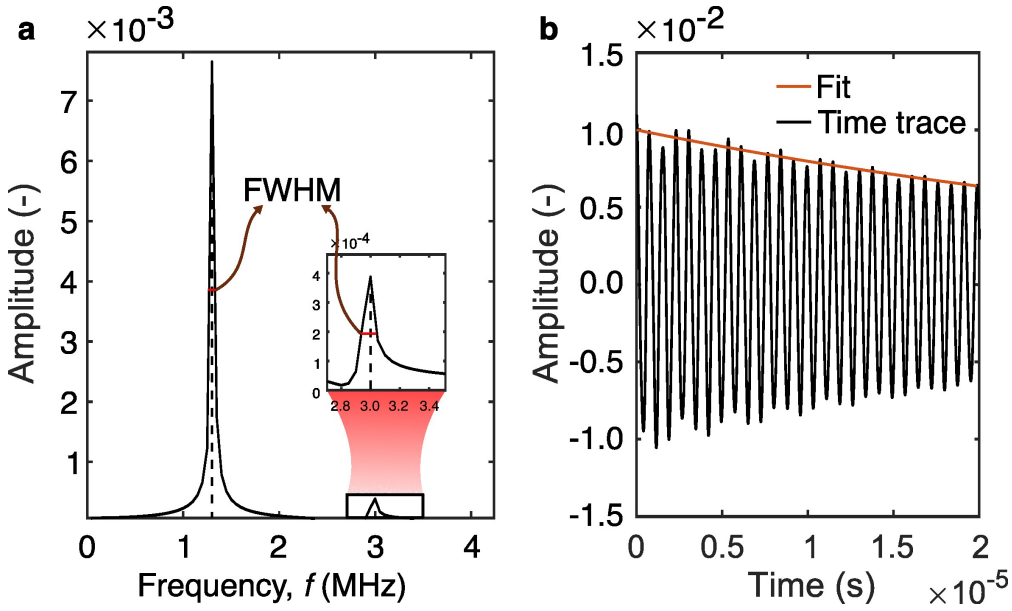

Supplementary Figure 6 | Frequency- and time-domain damping analysis.a, FFT of a typical time trace from a LIRAS experiment with two dominant modes. **b**, Time trace of a LIRAS experiment with an exponential fit over the envelope of the decay curve.

which simplifies to

$$\ddot{x} + \omega_0^2 x + 2\beta\dot{x} = 0, \tag{15}$$

where $\omega_0 = \sqrt{k/m}$ denotes the natural frequency of the system and $\beta = b/(2m)$ is the damping constant (both with dimensions of inverse time). Taking a solution to Eq. 15 of the form $x(t) = e^{rt}$ and assuming a weakly damped system with $\beta < \omega_0$ (representative of the LIRAS vibration waveforms shown in Fig. 1c), yields a solution

$$\begin{aligned} x(t) &= e^{-\beta t}\left(C_1 e^{i\omega_1 t} + C_2 e^{-i\omega_1 t}\right) \\ &= A e^{-\beta t}\cos(\omega_1 t - \delta), \end{aligned} \tag{16}$$

where A is the original amplitude of the signal and δ corresponds to a phase shift. As shown for a representative waveform obtained on an octet [100] 22-unit-cell-tall sample (Supplementary Fig. 6b), this model agrees with the response of metamaterials to photoacoustic excitation.

To obtain the damping factor, we opted to perform the damping measurements as half of the full-width at half maximum (FWHM) of the FFT peak corresponding to the longitudinal vibration mode. Namely, we relate the decay parameter for the FWHM as $2\beta = FWHM$, as shown in Supplementary Fig. 6a for the octet [100] 22-unit-cell sample. We also tested out the accuracy of an exponential fit enveloping the time trace to obtain the damping coefficients. To validate both equivalent approaches, we constructed a generic LIRAS time trace with two peaks whose frequencies, damping coefficients, and the ratio of amplitudes were taken from the LIRAS time trace of a $5 \times 5 \times 22$ octet [100] lattice. The FFT of this time trace is shown in Supplementary Fig. 6a where there are two dominant peaks at frequencies of $f_1 = 1.30$ MHz and $f_2 = 2.98$ MHz. The

values of the damping coefficients at these peaks obtained from the full width at half-maximum of the peak are $\beta_1 = 0.0229$ MHz and $\beta_2 = 0.0893$ MHz respectively. The amplitudes of the two peaks are in a ratio of 10:1. In Supplementary Fig. 6b we plot the time trace and fit a function of the form $y = Ae^{-\beta t}$ to the positive extremities of the waveform. From the fit, we obtain a value of $\beta = 0.0226$ MHz for the effective damping coefficient which is within 1% of β_1 indicating that this method can indeed be used to obtain the damping coefficient of the dominant mode. Conversely, the fact that the values obtained from fitting the decay function match the values obtained from FFT validates the accuracy of our analysis. Throughout our analysis, we elected to obtain damping properties from the frequency domain for two reasons: (i) it enabled focusing on a specific mode of interest (i.e., longitudinal), which is not guaranteed when doing the time-domain analysis and is also dependent on the relative dominance of a given mode compared to others, and (ii) it provided a more systematic route that was less susceptible to variability in fitting.

VI. Elastic Surface Computation

Supplementary Table 1 | LIRAS measurements of dynamic elastic properties of metamaterials in the MHz regime. TK-tetrakaidecahedron, Mono.-monolithic, Longi-longitudinal, Tor.-torsional, vel.-velocity, stiff.-stiffness, Dyn.-dynamic, sh.-shear.

	Octet [100]	Octet [110]	Octet [111]	TK [100]	TK [110]	TK [111]	Mono. IP-Dip
Longi. vel.(m/s)	800 ± 12	978 ± 7	979 ± 8	785 ± 19	692 ± 5	679 ± 12	2014 ± 47
Tors. vel.(m/s)	557 ± 50	–	–	321 ± 20	–	–	1135 ± 26
Dyn. stiff.(MPa)	127 ± 4	190 ± 3	191 ± 3	101 ± 5	78 ± 2	75 ± 3	4743 ± 26
Dyn. sh. stiff.(MPa)	47 ± 2	–	–	17 ± 3	–	–	1507 ± 70

In the experiments, we determine the effective stiffness of the metamaterials in [100], [110], and [111] directions and the shear stiffness in [100]. For a cubic crystal, the dynamic compliance tensor $\hat{\mathbb{S}}$ has the form

$$\hat{\mathbb{S}} = \begin{bmatrix} \hat{S}_{11} & \hat{S}_{12} & \hat{S}_{12} & 0 & 0 & 0 \\ \hat{S}_{12} & \hat{S}_{11} & \hat{S}_{12} & 0 & 0 & 0 \\ \hat{S}_{12} & \hat{S}_{12} & \hat{S}_{11} & 0 & 0 & 0 \\ 0 & 0 & 0 & \hat{S}_{44} & 0 & 0 \\ 0 & 0 & 0 & 0 & \hat{S}_{44} & 0 \\ 0 & 0 & 0 & 0 & 0 & \hat{S}_{44} \end{bmatrix}. \tag{17}$$

The directional stiffness $E_{\boldsymbol{d}}^*$ of such material along an arbitrary direction $\boldsymbol{d}$ with components (d_1, d_2, d_3) is related to the dynamic compliance tensor through the following relation:

$$E_{\boldsymbol{d}}^{*} = \frac{1}{\hat{S}_{11}\left[{d_1}^4 + {d_2}^4 + {d_3}^4\right] + 2\left(\hat{S}_{12} + 2\hat{S}_{44}\right)\left[(d_1 d_2)^2 + (d_2 d_3)^2 + (d_1 d_3)^2\right]}. \tag{18}$$

In Miller index notation, the direction stiffness along the Miller's directional indices $[hkl]$ is given by

$$\frac{1}{E_{[hkl]}^{*}} = \hat{S}_{11} + \left(2\hat{S}_{12} - 2\hat{S}_{11} + \hat{S}_{44}\right)\frac{\left(h^2k^2 + k^2l^2 + l^2h^2\right)}{(h^2 + k^2 + l^2)}. \tag{19}$$

Therefore, the three constants in compliance tensor ($\hat{S}_{11}$, $\hat{S}_{12}$ and $\hat{S}_{44}$) are related to the directional stiffness and dynamic shear stiffness through

$$\begin{cases} E_{[100]}^{*} = \frac{1}{\hat{S}_{11}} \\ E_{[110]}^{*} = \frac{2}{\hat{S}_{11}+\hat{S}_{12}+2\hat{S}_{44}} \\ E_{[111]}^{*} = \frac{3}{\hat{S}_{11}+2\hat{S}_{12}+\hat{S}_{44}} \\ G^{*} = \frac{1}{\hat{S}_{44}}, \end{cases} \tag{20}$$

where the dynamic shear stiffness G^{*} is determined by measuring the torsional wave velocity $c_T = 0.92\sqrt{\frac{G^{*}}{\rho}}$. Using the expressions in Eq. 20, we can obtain all the constants in the dynamic compliance matrix $\hat{\mathbb{S}}$. It is interesting to note that $\hat{S}_{12}$ can be obtained from both $E_{[111]}^{*}$ and $E_{[110]}^{*}$, enabling us to take the average of the two experiments. More accurate values for $\hat{S}_{12}$ can be obtained by measuring the directional stiffness along other directions. Therefore, we can calculate the elastic surface, i.e., the stiffness in any direction, for a cubic crystal from the dynamic compliance tensor through

$$E_{\boldsymbol{d}}^{*} = \frac{1}{\hat{\mathbb{S}}_{ijkl} d_i d_j d_k d_l}. \tag{21}$$

VII. Torsional Geometric Factor and Wave Velocity

Following the theory for torsional waves in slender rods[3], the torsional wave velocity is given by

$$c_T = \sqrt{\frac{GK}{\rho I_p}} \tag{22}$$

where G is the shear modulus, K is a geometric torsional factor, ρ is the density, and I_p is the polar area moment of inertia. For a rectangular cross-section (with width, w and height h), the geometric factor K is given by[3]

$$K = \frac{wh^3}{16}\left(\frac{16}{3} - 3.36\frac{h}{w}\left(1 - \frac{h^4}{12w^4}\right)\right). \tag{23}$$

To verify that this correction factor is valid for a lattice with a relative density $\bar{\rho}$, and elasticity tensor $\hat{\mathbb{C}}$, we performed finite element analysis on a rod with dimensions 37.5 μm × 37.5 μm × 150 μm. For a rod with arbitrary cross-section under torsion, the angular displacement, θ and moment, T are related as

$$\theta = \frac{LT}{KG}, \tag{24}$$

where L is the length of the rod, G is the shear modulus, K is the geometric torsional factor. We applied a homogenous rotation gradient to the rod where the rotation of each section is given by

$$\theta(x) = \theta_o \frac{x}{L}, \tag{25}$$

where x is the position along the axis of the rod and θ_o is the rotation at $x = L$.

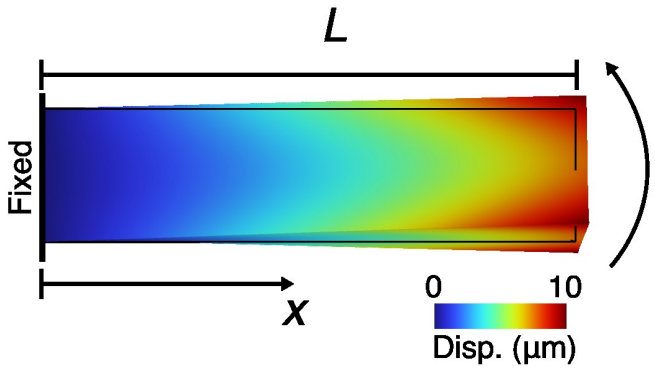

Supplementary Figure 7 | FEM validation of torsional factor for octet metamaterials. Simulation of a square rod with the constituent (anisotropic) elastic properties of an octet lattice (derived through static homogenization), subjected to uniform angular displacement gradient.

We calculated the reaction moment on the section at $x = L$ and obtained the corresponding geometric factor K. We then verified that the value of K obtained from FEA matched that obtained from Eq. 23 to within 2%. Since all samples in this study have a square cross-section, the expression simplifies to $K = 0.140833h^4$. Note that in applying this simplification, we are treating the octet and tetrakaidecahedron metamaterials as an effective continuum, a valid assumption for our sample design per the analysis presented in Extended Data Fig. 2. Applying the expression for the polar area moment of inertia for a square cross-section, $I_p = h^4/6$, thus yields a simplified expression for the torsional wave velocity

$$c_T = \sqrt{\frac{6 \cdot G \cdot 0.140833h^4}{\rho h^4}} = 0.919238\sqrt{\frac{G}{\rho}}. \tag{26}$$

VIII. Inertial Stiffening of Metamaterial Architectures

To explain this difference in dynamic stiffening, we performed explicit dynamic FEA simulations on octet and tetrakaidecahedron unit cells with relative densities of $\overline{\rho}_{Oc}$ =17% and $\overline{\rho}_{Tk}$ =14%, respectively. We performed uniaxial compression by imposing a strain rate, $\dot{\varepsilon}_{zz} = 60\ s^{-1}$ to the geometry. From Supplementary Fig. 8 we observe the volume-averaged maximum absolute principal logarithmic strain is comparable for both tetrakaidecahedron and octet morphologies, indicating that the rate-dependent constituent-material stiffening should be the same for both geometries. However, we notice the average acceleration of the two geometries is different. Specifically, the average acceleration of octet is 6.95×10^8 mm/s^2 while that of the tetrakaidecahedron is 9.16×10^8 mm/s^2. This indicates that there are higher inertial forces experienced by the tetrakaidecahedron compared to the octet. To quantitatively relate this to the dynamic stiffening observed in both geometries, we take a closer look at equilibrium on both unit cells. By ignoring the inherent material stiffening and assuming the unit cell to have elastic static stiffness k, we obtain

$$k_{eff}u = ku + ma, \tag{27}$$

where k_{eff} is the effective dynamic stiffness of the geometry, u is the applied displacement, m is the mass of the geometry, and a is the acceleration within the geometry. Therefore, the stiffening, η_{stiff} of each geometry is given by

$$\eta_{stiff} = \frac{k_{eff} - k}{k} = \frac{ma}{ku}. \tag{28}$$

The ratio of stiffening between octet and tetrakaidecahedron is thus expressed as

$$\frac{\eta_{stiff,Oc}}{\eta_{stiff,Tk}} = \frac{m_{Oc}a_{Oc}k_{Tk}}{m_{Tk}a_{Tk}k_{Oc}}, \tag{29}$$

with the ratio of masses expressed as $m_{Oc}/m_{Tk} = \overline{\rho}_{Oc}/\overline{\rho}_{Tk}$. Therefore, the ratio of stiffening becomes

$$\frac{\eta_{stiff,Oc}}{\eta_{stiff,Tk}} = \frac{m_{Oc}}{m_{Tk}} \cdot \frac{a_{Oc}}{a_{Tk}} \cdot \frac{k_{Tk}}{k_{Oc}} = \frac{0.17}{0.14} \cdot \frac{6.95 \times 10^8}{9.16 \times 10^8} \cdot \frac{50}{84} = 0.55, \tag{30}$$

where the elastic static stiffness was obtained from static simulations on the same geometries. From LIRAS measurements, we determined the dynamic stiffening to be ~40% for the octet and ~96% for the tetrakaidecahedron, yielding a stiffening ratio of 0.4/0.96 = 0.42. While our simple dynamic simulations do not account for rate-dependent material properties, this remarkable agreement between theoretical equilibrium arguments and experimental values confirms the importance of architecture-dependent inertial forces.

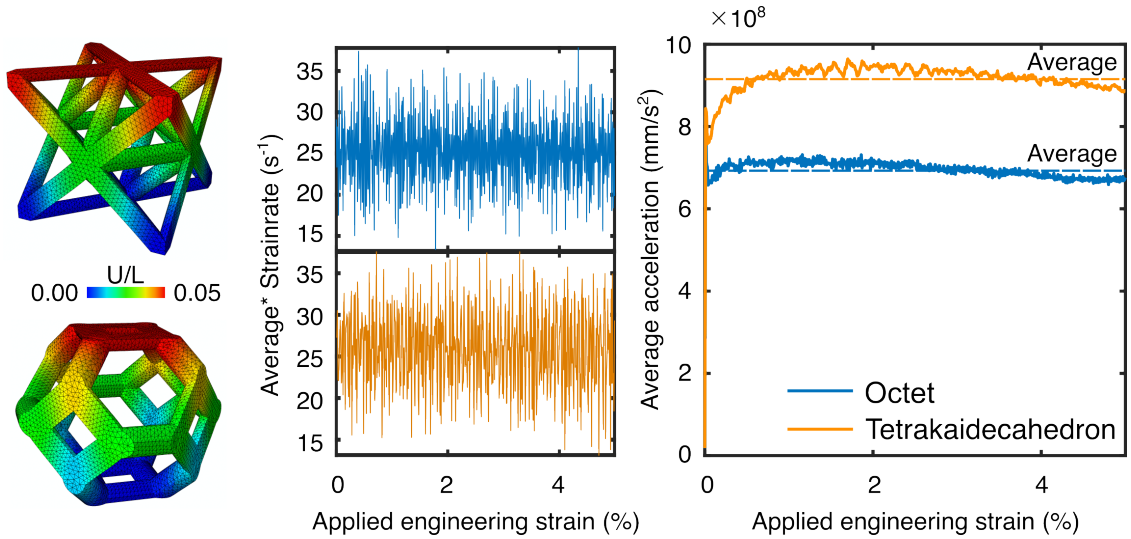

Supplementary Figure 8 | Explicit dynamics simulations of both metamaterial architectures. Displacement field at 5% applied engineering strain for octet and tetrakaidecahedron (left). Volume-averaged maximum absolute principal logarithmic strain rate vs. applied engineering strain for octet and tetrakaidecahedron morphologies (center). Average acceleration as a function of time for octet and tetrakaidecahedron morphologies (right), indicating higher inertial contributions in the tetrakaidecahedron.

IX. Defective-Sample Spectra

Here, we present the evolution of spectra as the defect density in metamaterial samples increased. In the case of bulk inclusions in octet metamaterials (Supplementary Fig. 9a), the higher-frequency peak (corresponding to a longitudinal mode) gradually shifted to higher frequencies prior to a jump where inclusion-percolation likely occurred. For the missing-beam octahedron metamaterials (Supplementary Fig. 9b), the longitudinal-mode peak gradually decreased in frequency. As the defect density increased, loss of symmetry due to randomly distributed defects gave rise to stronger flexural modes (lower frequency peaks), despite a center-pump scheme being employed.

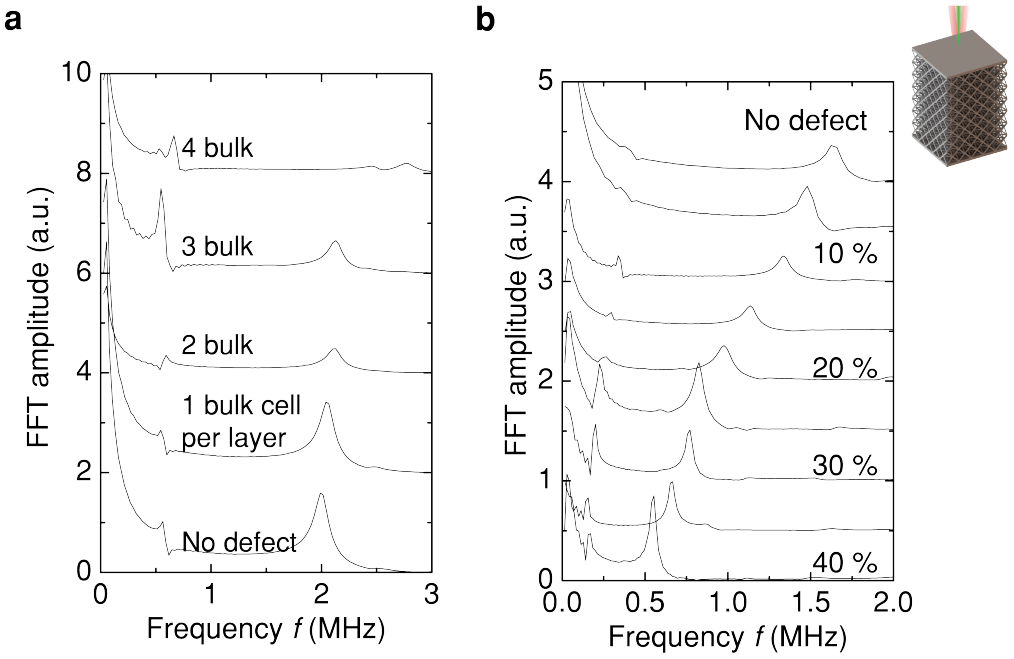

Supplementary Figure 9 | FFT spectra of defect samples. **a**, FFT spectra of inserted bulk cells into an octet lattice. **b**, FFT spectra of missing beams in an octahedron lattice.

To further validate the defect-quantification capabilities of LIRAS, we conducted supplementary experiments and simulations on a lattice architecture known as the "braced cubic" geometry. This lattice structure exhibits both stretching- and bending-dominated deformations depending on its orientation, thereby lacking a single dominant deformation mode. As shown in Supplementary Fig. 10a, loading along the [100] direction leads to more uniform stress contours that indicate a stretching-dominated response, while Supplementary Fig. 10b shows significant stress gradients in the diagonal struts that indicate a bending-dominated response along the [111] direction.

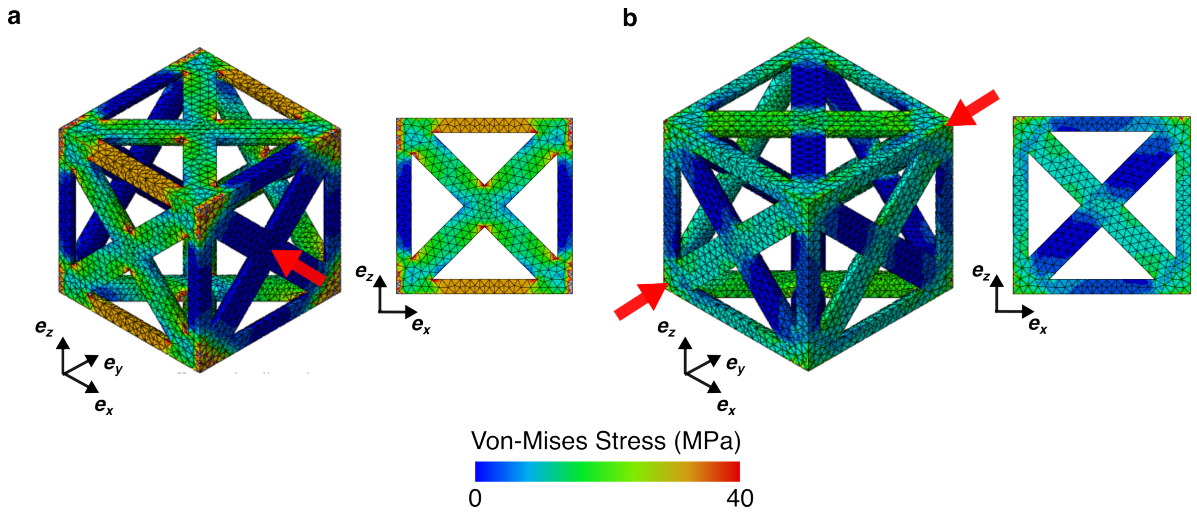

Supplementary Figure 10 | Mixed stretching and bending deformation in braced cubic morphology. Stress contours of a braced-cubic unit cell compressed in the **a**, [100] direction, **b**, [111] direction.

To demonstrate that LIRAS capabilities are architecture- and deformation-mode-agnostic, we performed experiments on the braced cubic geometry with varying magnitudes of defects, as shown in Supplementary Fig. 11. These experiments validate the results reported in Fig. 5 for the octahedron geometry, namely, eigenfrequencies decrease with increasing density of missing beams.

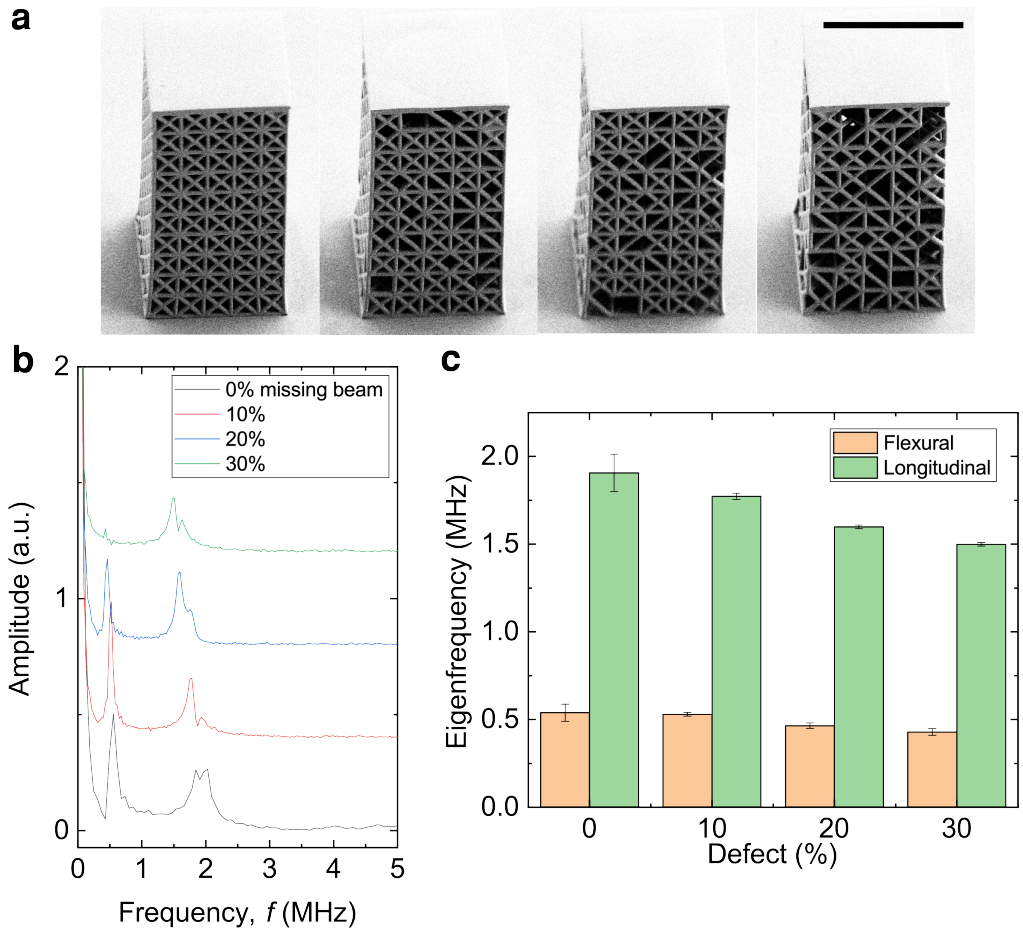

Supplementary Figure 11 | Vibrational defect identification in braced cubic metamaterials. **a**, SEM images of braced cubic (BC) metamaterials of $5 \times 5 \times 10$ unit-cell tessellation. The BC lattices from left to right possess 0, 10, 20, and 30% missing beams. Black scale bar, 50 μm. **b**, Measured eigenvibration spectra for all samples. **c**, Measured shift in longitudinal and flexural eigenfrequencies, denoting a decrease in frequencies as a function of defect density.

We have also conducted an investigation on defective octet metamaterials, displayed in Fig. 12. These experiments are consistent with the trend that eigenfrequencies decrease with increasing density of missing beams.

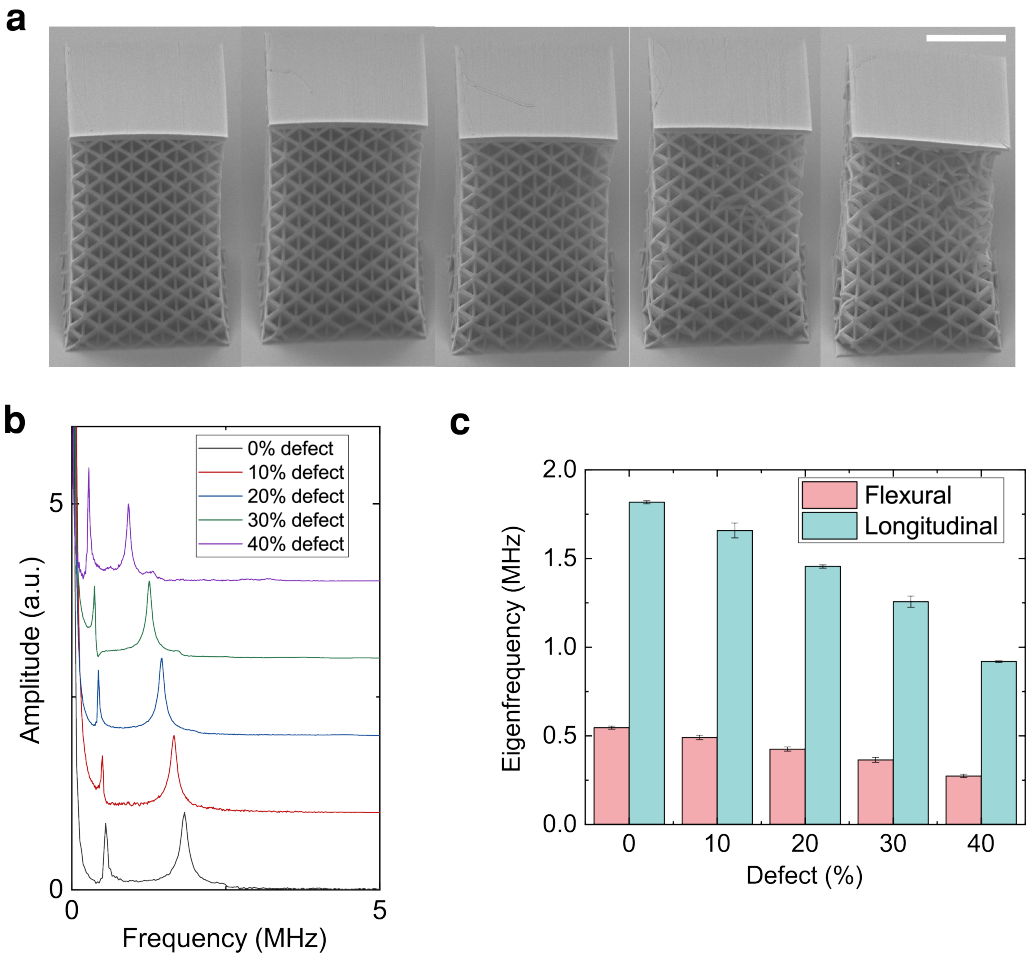

Supplementary Figure 12 | Vibrational defect identification in octet metamaterials. **a**, SEM images of octet metamaterials of $5 \times 5 \times 10$ unit-cell tessellation. The octet lattices from left to right possess 0, 10, 20, 30, and 40% missing beams. White scale bar, 25 μm. **b**, Measured eigenvibration spectra for all samples. **c**, Measured shift in longitudinal and flexural eigenfrequencies, denoting a decrease in frequencies as a function of defect density.

X. Comparison of Different Techniques to Measure Mechanical Properties

To elucidate the advantages of our LIRAS technique compared to established micro- and nanomechanical characterization techniques, we constructed Supplementary Table 2 below. Here, *Non-contact* denotes a technique's ability to perform measurements without attaining physical contact with a sample, *Non-damaging* determines whether permanent damage on the sample occurs upon measurement, *Spatial res.* provides an estimate of the minimum measurable sample displacement, *Temporal res.* denotes the techniques' temporal resolution, *Attenuation character.* indicates a technique's ability to provide signal attenuation measurements, and *Shear char.* indicates the ability to obtain shear elastic properties.

Techniques	Non-contact	Non-damaging	Spatial res.	Temporal res.	Attenuation character.	Shear char.	Ref.
Piezo-excitation with imaging	No	Yes	~ 10 nm	~ 10 ns	No	No	[4]
Fluid-mediated ultrasonics	Yes	Yes	N/A	~ 1 ns	Yes	No	[5]
Unixial compression	No	No	~ 1 nm	~ 1 μs	No	No	[6]
Kolsky bar	No	No	~ 100 nm	~ 1 μs	No	No	[7]
Resonant ultrasound spectroscopy	Yes	Yes	~ 10 nm	~ 1 ns	No	Yes	[8]
Surface acoustic spectroscopy	Yes	Yes	~ 10 nm	~ 1 ns	No	Yes	[9]
LIRAS	Yes	Yes	~ 1 nm	~ 1 ns	Yes	Yes	

Supplementary Table 2 | Comparison between existing micro- and nanomechanical characterization techniques and our LIRAS framework. Spatial resolution refers to the minimum sample displacement that leads to measurable results.

Supplementary References

1.Christ Glorieux, JD Beers, El Hassane Bentefour, K Van de Rostyne, and Keith A Nelson. Phase mask based interferometer: Operation principle, performance, and application to thermoelastic phenomena. *Review of scientific instruments*, 75(9):2906–2920, 2004.

2.J.R. Taylor. *Classical Mechanics*. G - Reference,Information and Interdisciplinary Subjects Series. University Science Books, 2005.

3.Karl F Graff. *Wave Motion in Elastic Solids*. Dover Books on Physics. Dover Publications, 2012.

4.Tobias Frenzel, Julian Köpfler, Erik Jung, Muamer Kadic, and Martin Wegener. Ultrasound experiments on acoustical activity in chiral mechanical metamaterials. *Nature Communications*, 10(1):3384, 2019.

5.Gunho Kim, Carlos M Portela, Paolo Celli, Antonio Palermo, and Chiara Daraio. Poroelastic microlattices for underwater wave focusing. *Extreme Mechanics Letters*, 49:101499, 2021.

6.Carlos M Portela, A Vidyasagar, Sebastian Krödel, Tamara Weissenbach, Daryl W Yee, Julia R Greer, and Dennis M Kochmann. Extreme mechanical resilience of self-assembled nanolabyrinthine materials. *Proceedings of the National Academy of Sciences*, 117(11):5686–5693, 2020.

7.Daniel T Casem, John J Pittari, and Jeffrey J Swab. High-rate indentation using miniature kolsky bar methods. In *Dynamic Behavior of Materials, Volume 1: Proceedings of the 2021 Annual Conference and Exposition on Experimental and Applied Mechanics*, pages 63–65. Springer, 2022.

8.P Sedlák, H Seiner, J Zídek, M Janovská, and M Landa. Determination of all 21 independent elastic coefficients of generally anisotropic solids by resonant ultrasound spectroscopy: benchmark examples. *Experimental Mechanics*, 54:1073–1085, 2014.

9.Paul Dryburgh, Wenqi Li, Don Pieris, Rafael Fuentes-Domínguez, Rikesh Patel, Richard J Smith, and Matt Clark. Measurement of the single crystal elasticity matrix of polycrystalline materials. *Acta Materialia*, 225:117551, 2022.